Noname manuscript No.
(will be inserted by the editor)

Characterization of the retinal changes of the 3×Tg-AD mouse model of Alzheimer's disease

Hugo Ferreira · João Martins · Ana Nunes · Paula I. Moreira · Miguel Castelo-Branco · António Francisco Ambrósio · Pedro Serranho · Rui Bernardes

Received: date / Accepted: date

Abstract Alzheimer's disease (AD) is a progressive neurodegenerative disorder whose diagnosis remains a notable challenge. The literature suggests that cerebral changes precede AD symptoms by over two decades, implying a significantly advanced stage of AD by the time it is usually diagnosed. In the study herein, texture analysis was applied to computed optical coherence tomography ocular fundus images to identify differences between a group of the transgenic mouse model of the Alzheimer's disease (3×Tg-AD) and a group of wild-type mice, at the ages of one and two-months-old. A substantial difference between groups was found at both time-points across all neuroretina's layers. Here, the inner nuclear layer stands out both in the level of statistically significant differences and on the extension of these differences which span through the imaged area. Also, the progression of AD is suggested to be spotted by

H. Ferreira, J. Martins, A. Nunes, M. Castelo-Branco, P. Serranho, R. Bernardes
Coimbra Institute for Biomedical Imaging and Clinical Research (CIBIT)
Institute of Nuclear Sciences Applied to Health (ICNAS)
University of Coimbra, Portugal

J. Martins, P. I. Moreira, A. F. Ambrósio
Center for Innovative Biomedicine and Biotechnology (CIBB), University of Coimbra, Portugal

P. I. Moreira, M. Castelo-Branco, A. F. Ambrósio, R. Bernardes
Faculty of Medicine, University of Coimbra, Portugal

A. F. Ambrósio
Coimbra Institute for Clinical and Biomedical Research (iCBR)
Faculty of Medicine, University of Coimbra, Portugal
E-mail: afambrosio@fmed.uc.pt

P Serranho
Mathematics Section, Department of Science and Technology, Universidade Aberta, Portugal

Corresponding author: R. Bernardes – rmbernardes@fmed.uc.pt

texture analysis as demonstrated by the significant difference found in the inner plexiform and the outer nuclear layers from the age of one to the age of two-months-old. These findings demonstrate the potential of the use of the retina and texture analysis to the diagnosis of AD and monitor AD progression. Besides, the differences between groups found in this study suggest that the 3×Tg-AD model may be inappropriate to study early changes associated with the AD and other animal models should be tested following the same path and rationale. Moreover, these results also suggest that the human genes present in these transgenic mice may have an impact on the neurodevelopment of offsprings which would justify the significant changes found at the age of one-month-old.

Keywords optical coherence tomography · retina · biomarkers · texture analysis · Alzheimer's disease · mouse model · 3×Tg-AD · early diagnosis

Declarations

Funding: This study was funded by The Portuguese Foundation for Science and Technology (FCT) throught PTDC/EMD-EMD/28039/2017, PEst-UID/NEU/04539/2019, UID/Multi/04621/2013 and UID/04950/2017, and by FEDER-COMPETE through POCI-01-0145-FEDER-028039 and POCI-01-0145-FEDER-007440.

Conflict of interest: The authors of this paper declare no conflict of interest.

Ethics approval: This study was approved by the Animal Welfare Committee of the Coimbra Institute for Clinical and Biomedical Research (iCBR), Faculty of Medicine, University of Coimbra. All procedures involving mice were conducted as per the Association for Research in Vision and Ophthalmology statement for animal use, and in agreement with the European Community Directive Guidelines for the care and use of non-human animals for scientific purposes (2010/63/EU), transposed into the Portuguese law in 2013 (DL113/2013).

Consent to participate: Not applicable.

Consent to publication: Not applicable.

Availability of data and material: Not available.

Code availability: Not available.

Noname manuscript No.
(will be inserted by the editor)

Characterization of the retinal changes of the 3×Tg-AD mouse model of Alzheimer's disease

Abstract Alzheimer's disease (AD) is a progressive neurodegenerative disorder whose diagnosis remains a notable challenge. The literature suggests that cerebral changes precede AD symptoms by over two decades, implying a significantly advanced stage of AD by the time it is usually diagnosed. In the study herein, texture analysis was applied to computed optical coherence tomography ocular fundus images to identify differences between a group of the transgenic mouse model of the Alzheimer's disease (3×Tg-AD) and a group of wild-type mice, at the ages of one and two-months-old. A substantial difference between groups was found at both time-points across all neuroretina's layers. Here, the inner nuclear layer stands out both in the level of statistically significant differences and on the extension of these differences which span through the imaged area. Also, the progression of AD is suggested to be spotted by texture analysis as demonstrated by the significant difference found in the inner plexiform and the outer nuclear layers from the age of one to the age of two-months-old. These findings demonstrate the potential of the use of the retina and texture analysis to the diagnosis of AD and monitor AD progression. Besides, the differences between groups found in this study suggest that the 3×Tg-AD model may be inappropriate to study early changes associated with the AD and other animal models should be tested following the same path and rationale. Moreover, these results also suggest that the human genes present in these transgenic mice may have an impact on the neurodevelopment of offsprings which would justify the significant changes found at the age of one-month-old.

Keywords optical coherence tomography · retina · biomarkers · texture analysis · Alzheimer's disease · mouse model · 3×Tg-AD · early diagnosis

1 Introduction

Diagnosis of Alzheimer's disease (AD) remains a major challenge. Simple diagnostic to identify early biomarkers for tracking the onset and progression of AD would be

of utmost importance. In the USA alone, 5.6 million people aged 65 and older lived with AD in 2019, that is, one in ten people (10%) in this age-group [1]. With the increase of life expectancy for the world's population, 64.2 years in 1990, 72.6 years in 2019 and 77.1 years expected in 2050 [2], the prospect is to an increase in the population with AD in the near future, even though epidemiological evidence suggests a potential reduction in dementia incidence [3].

Based on Pittsburgh Compound-B (PiB) studies, it is hypothesised that cerebral changes precede AD symptoms by over two decades [4,5]. This substantial period implies a significantly advanced stage of AD by the time it is usually diagnosed. Furthermore, a definite diagnosis can only be performed post-mortem [6]. These challenges make it difficult to access the first pathophysiological changes caused by AD and to track their progress during the prodromal stages of the disease.

An alternative diagnostic approach that gained momentum in recent years is the use of the retina as a window into the brain [7,8]. The supporting rationale is that the retina and the brain have the same embryonic origin [5], which makes the retina the only part of the central nervous system (CNS) directly accessible through non-invasive optical means. This hypothesis allows performing non-invasive studies, *in vivo* and *in situ*, at any time along the lifespan of the person or animal being studied.

Conflicting reports exist on the findings of one of the hallmarks of AD, the accumulations of Amyloid-β ($A\beta$), in the retina [9]. Other biomarkers of AD were studied based on the hypothesis that AD is a vascular disorder [10]. Alternative biomarkers were also put forward, like the thinning of the retinal nerve fibre layer (RNFL) in the eyes of AD patients [11,12]. Here, a particularly confounding factor is the fact that RNFL thinning is not exclusive to AD [13].

We have put forward alternative biomarkers based on the analysis of computed fundus images for individual layers of the retina [14]. Also, we recently demonstrated that texture biomarkers allow not only to distinguish AD patients from age-matched healthy controls correctly but also to distinguish them from age-matched Parkinson's disease patients [15], thus demonstrating the potential of texture biomarkers for the study of neurodegenerative disorders [16].

To address the fundamental question of whether the retina holds vital information towards AD diagnosis and, if so, how early can changes be identified, an ongoing project is imaging triple-transgenic mouse model of AD (3$\times$Tg-AD) mice since they express three major genes associated with familial AD, namely APPswe, PS1M146V, and tauP301L, and develop the pathological hallmarks of disease in an age-dependent manner [17,18]. These animals are being imaged from the age of one-month-old, every month up to the age of four-months-old, at six-months-old, and every six months after that until the age of 24-months-old. Preliminary results using this mouse model [19,20] suggest that texture analysis can be successfully used for this purpose.

As part of the research project mentioned above, in this work, we identify the texture features that present statistically significant differences between the mouse model of AD and the healthy control groups, at the ages of one and two-months-old, and report the image processing steps towards the computation of these features.

2 Materials and methods

2.1 Sample and study groups

The mouse model of AD used in this work is the 3×Tg-AD, while the healthy control mice used for comparison are wild-type (WT) mice (C57BL6/128S background).

This study was approved by the Animal Welfare Committee of the Coimbra Institute for Clinical and Biomedical Research (iCBR), Faculty of Medicine, University of Coimbra. All procedures involving mice were conducted as per the Association for Research in Vision and Ophthalmology statement for animal use, and in agreement with the European Community Directive Guidelines for the care and use of non-human animals for scientific purposes (2010/63/EU), transposed into the Portuguese law in 2013 (DL113/2013).

Optical coherence tomography (OCT) data was gathered (when possible) from both eyes of 35 WT and 35 3×Tg-AD mice. This would provide 70 eye scans per group. However, some were excluded from the study due to poor image quality, yielding a total of 68 and 65 eye scans, respectively for the WT and the 3×Tg-AD groups, for the age of one-month-old and, 60 and 64 eye scans at the age of two-months-old.

2.2 Data acquisition and characterization

Mice were imaged by the Micron IV OCT System (Phoenix Research Labs, Pleasanton, CA, USA). All eye volume scans, made of 512 non-compressed B-scans TIFF files (of 512 A-scans each), were taken at the same retinal location, horizontally centred on the optic disc and vertically above the optic disc's border.

OCT B-scan images allow distinguishing between several retinal layers in a way that each visible retinal layer corresponds to histological reports of the retina [21,22]. However, from a computational point-of-view, retinal layer segmentation from OCT data is hampered by the low signal-to-noise ratio (SNR), common in this data. The main reason is speckle noise, intrinsic to low-coherence interferometry techniques, which cannot wholly be removed by digital means. To this end, some pre-processing techniques are applied in order to improve the quality of the segmentation.

2.3 OCT data pre-processing

Data used in this work was pre-processed in two steps, aiming to centre and align the location of the retina within each B-scan. This normalization allows us to know, *a*

priori, the rough location of the different retinal layers, which will stretch horizontally along the B-scan. Mice, as opposed to humans, do not possess macula, leading to homogeneous layer thickness throughout the imaged retina.

Two average A-scans (avgA) are computed for each B-scan, one for the left and another for the right halves of the B-scan. Each is then low-pass filtered to achieve only two local maxima (Fig. 1), one due to the hyper-reflectivity of the RNFL and one due to the hyper-reflectivity of the retinal pigmented epithelium (RPE), respectively the left and right peaks shown in figure 1.

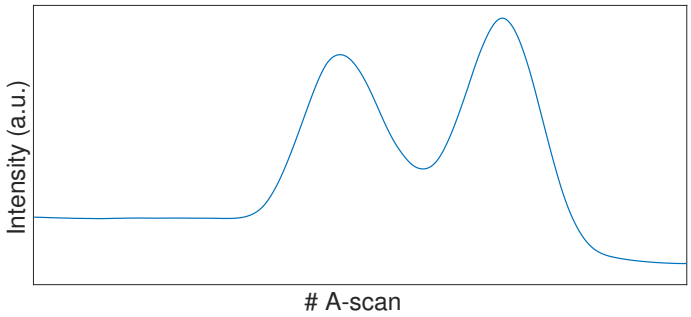

Fig. 1: Example of an average A-scan low-pass filtered (vitreous, retina and choroid - from left to right). Two distinct peaks are present, one due to the retinal nerve fibre layer (RNFL - left peak) and one due to the retinal pigment epithelium (RPE - right peak).

One then determines the midpoints between the two peaks for each of the left and right half average A-scans and determines the line that crosses both of them, as illustrated in orange in figure 2 (left). Then each A-scan of the B-scan is shifted (in the depth direction) so that this line becomes horizontal in a predefined depth position (in red, in figure 2), as illustrated in figure 2 (right).

2.4 Retinal interface detection

Many segmentation methods for OCT data have been reported [23, 24], most for OCT data of human retinas. However, these do not perform well when applied to mouse retinas because of the low contrast between retinal layers when compared to humans. Furthermore, because the mouse retina does not have a macula/foveal depression, retinal layers present a homogeneous thickness, and all retinal layers are present in the entire data volume of the OCT.

Taking advantage: 1) of the homogeneous thickness of each retinal layer across each B-scan; 2) that consecutive layers present distinct intensity levels, and; 3) of the horizontal distribution of the layers following the pre-processing steps, we compute a local metric defined by:

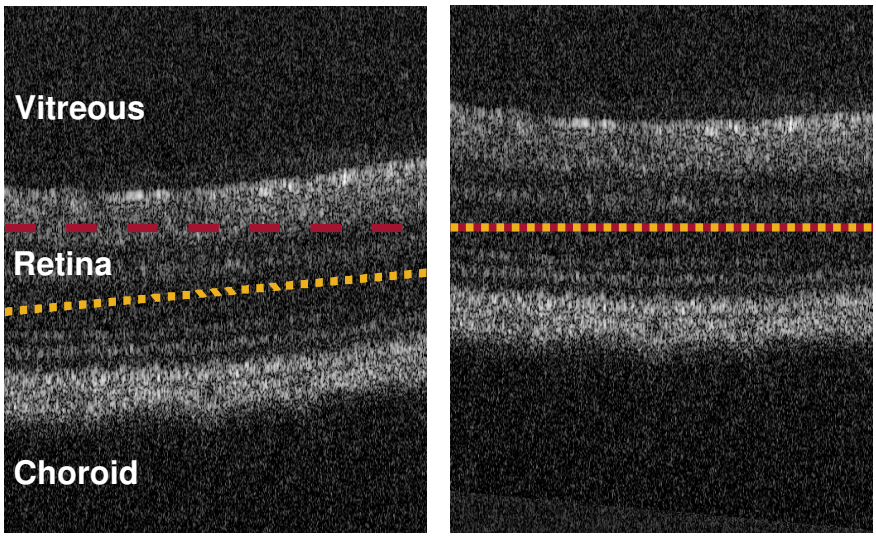

Fig. 2: B-scan pre-processing (cropped for the ease of visualisation). Before (left) and after (right) the pre-processing. The red dashed line shows the predefined location to align all A-scans from the B-scan, and the orange dotted line shows the middle position of the retina.

$$R(i,j) = \frac{C^u(i,j)}{C^d(i,j)}, \tag{1}$$

at each B-scan's pixel. To speed up the process and because the location of the retina within the B-scan is approximately known, after the pre-processing, this process can be run only in the region of interest within the B-scan.

The metric defined in (1) is the ratio of the convolution of the B-scan image (I) with the two kernels, of size $M \times N$, defined in (2) and (3), respectively, ω^u and ω^d, with $C^\gamma = I * \omega^\gamma$, $\gamma = \{u,d\}$.

$$\omega^u(s,t) = \begin{cases} 1, & 0 \geq t \geq \frac{N}{2} \quad \text{and} \quad \frac{M}{N}t \leq s \leq -\frac{M}{N}(t-N) \\ 0, & otherwise \end{cases}, \tag{2}$$

$$\omega^d(s,t) = \begin{cases} 1, & \frac{N}{2} \geq t \geq N \quad \text{and} \quad -\frac{M}{N}(t-N) \leq s \leq \frac{M}{N}t \\ 0, & otherwise \end{cases}, \tag{3}$$

where (3) is the 180-degree rotation of (2).

Filtering each B-scan with any of these kernels produces a scaled version of a low-pass filtered B-scan with the scaling parameter canceling out by the ratio. The ratio R (1) presents a maximum for transitions from hyper- to hypo-reflective layers, and a minimum for transitions from hypo- to hyper-reflective layers, in the top to bottom direction. This is illustrated in figure 4. The size of the kernel used was adjusted to the thickness of the layers at hand, and the triangular shape allows avoiding the influence

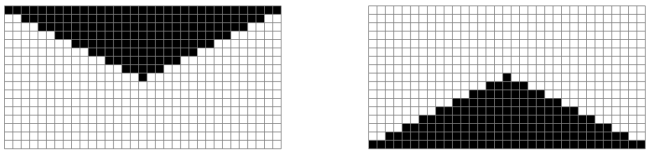

Fig. 3: Filters' kernels used. The left shows the kernel for the top layer and the right shows the kernel for the bottom layer. The ratio between the result of these filters allows determining the interfaces of the retinal layers. Filter values: black - 1, white - 0.

of immediate neighboring A-scans at the interface location, accommodating small local variations of the interface to the horizon.

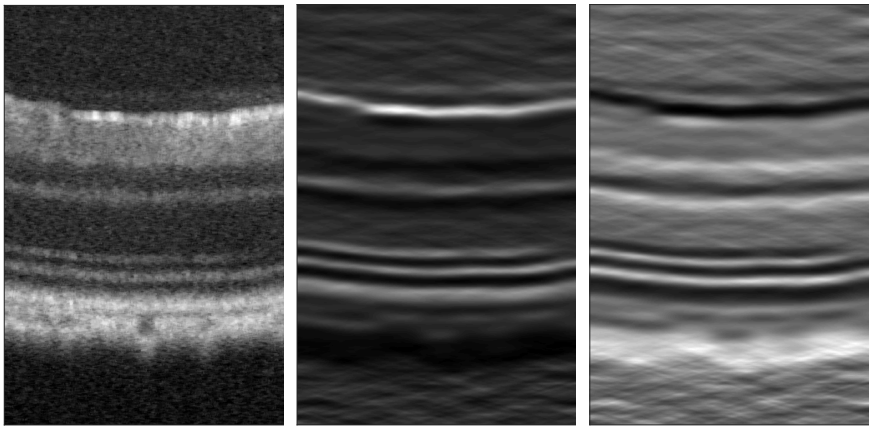

Fig. 4: Left: cropped B-scan for the ease of visualisation. Middle: the image of R (1). Right: the image of R^{-1} (1).

2.5 Segmentation

The histology of the mouse retina is well known and well documented in the literature [21,22]. Therefore, the number of retinal layers and their characteristics, including their average thickness, and the relation between the thickness of different layers is well known. Also, the layered structure of the retina is evident in the B-scan images, as shown in figure 4. At the interfaces between layers, there is a transition in the intensity level from one layer to the next, which matches with local maximum/minimum of R, as defined in (1).

The segmentation of each B-scan is processed in three steps. First, two interfaces are determined, one corresponding to the transitions between the vitreous and the RNFL – the inner limiting membrane (ILM) –, and the interface between the outer segment of the photoreceptors (OS) and the RPE – the OS-RPE –, as the RNFL and the RPE are the most hyper-reflective layers in the retina.

The second step uses the interface OS-RPE as a starting point to search for the location of the interface between the outer nuclear layer (ONL) and the inner segment of the photoreceptors (IS) – ONL-IS – as the one presenting a local maximum in the R mapping (Eq. 1) as shown in figure 4 (centre). Having determined the ILM and the ONL-IS interfaces, the region of the retina for analysis within this work, the neuroretina, is now well established.

Finally, the remaining interfaces between the layers of the neuroretina – the RNFL, the ganglion cell layer (GCL), the inner plexiform layer (IPL), the inner nuclear layer (INL), the outer plexiform layer (OPL), and the ONL –, can now be estimated resorting to the knowledge of the relation between the thickness of these layers, drawn from histological studies [21,22], by mapping their relations to the region of the B-scan within the established limits.

The result of this approach can be seen in figure 5, where the mapping mentioned above determined the additional interfaces.

2.6 Texture features of OCT data

Texture provides information on the spatial distribution of pixels' intensity in a region or a whole image, for both grayscale and colour [25]. In general, two types of texture can be considered: pattern texture and random texture. While the first exhibits a visible regularity, the latter does not [25].

For each of the segmented layers, a mean-value fundus (MVF) image [14] was computed as the average of the A-scan values between the boundaries of the layer, i.e. none of the remaining A-scan values is taken into account.

MVF images were split into squared blocks of 20 pixels each, to capture local texture information, yielding 24×24 blocks per image, therefore cropping MVF images from their original 512×512 pixels size to 480×480 pixels, discarding pixels from the borders of the image. Also, the number of grayscale levels of the images was reduced from 65536 (16 bits) to 16 (4 bits).

The Gray-Level Co-occurrence Matrix (GLCM) [26] was used to determine texture information for each block. Furthermore, four directions (0°, 45°, 90° and 135°) with symmetry ON (i.e., 180° apart angles are considered the same) and scale (pixel distance) of one pixel, led to four GLCMs per block. For each of these, 20 features were determined: a) Inverse Difference Moment/Energy, b) Contrast/Inertia, c) Correlation, d) Angular Second Moment/Uniformity, e) Sum Average, f) Sum of Squares, g) Sum Variance, h) Sum Entropy, i) Difference Variance, j) Difference Entropy, k) Information Measure of Correlation 1 (IMC1), l) Information Measure of Correlation 2 (IMC2), m) Entropy, n) Dissimilarity, o) Autocorrelation, p) Maximum Probability, q) Cluster Prominence, r) Cluster Shade, s) Inverse Difference Normalized (INN) and t) Inverse Difference Moment Normalized (IDN). These are defined in [26] (a to

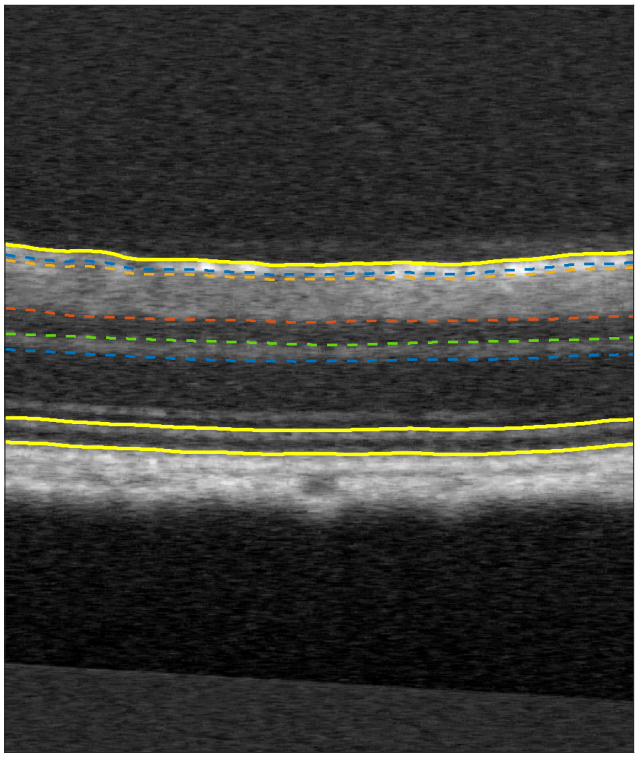

Fig. 5: Result of the segmentation process. Solid yellow lines show the segmented interfaces. Dashed lines show the interfaces as determined based on the average layer thickness for mice – drawn from known histology [21,22].

m), [27] (n), [28] (o and p), [29] (q and r), and [30] (s and t). Each feature is considered as the maximum across the four directions to decouple features' values from the orientation, resulting in 20 features per block.

Blocks were then aggregated into quadrants by defining each quadrant feature's value as the average of 12×12 blocks. In this way, a total of 480 features (20 features $\times$ 4 quadrants $\times$ 6 layers) characterize each retina.

2.7 Statistical analysis

The Kolmogorov-Smirnov normality test was applied to the 480 features to test normality in each group. Since the results indicated that the distributions are not normal for most features, we used the non-parametric Mann-Whitney test to determine differences between WT and 3$\times$Tg-AD groups, considering significance levels of 5%, 1%, and 0.1%.

All data processing was performed using Matlab R2018a (The MathWorks Inc., Natick, MA, USA), and the statistical treatment was made using IBM SPSS 25.

3 Results

The number of features with significant statistical differences between groups, per layer and time-point, are presented in table 1.

Please note that the number of features disclosed takes into account the same feature if it is present - that is, showing statistically significant differences between groups - in different quadrants. For example, the *Entropy* at RNFL at the age of one-month-old (Table 2) shows differences in two quadrants and therefore is counted twice in tables 1 and 3.

Table 1: Number of significant features per layer, at the ages of one and two-months-old. The total number of features per layer is 80.

	One month old			Two months old		
	Number of Significant Features			Number of Significant Features		
	$p \leq 0.001$	$p \leq 0.01$	$p \leq 0.05$	$p \leq 0.001$	$p \leq 0.01$	$p \leq 0.05$
RNFL	19 (23.8%)	29 (36.3%)	35 (43.8%)	29 (36.3%)	32 (40.0%)	39 (48.8%)
GCL	27 (33.8%)	38 (47.5%)	50 (62.5%)	40 (50.0%)	52 (65.0%)	61 (76.3%)
IPL	25 (31.3%)	38 (47.5%)	47 (58.8%)	45 (57.5%)	59 (73.8%)	66 (82.5%)
INL	48 (60.0%)	61 (76.3%)	69 (86.3%)	59 (73.8%)	67 (83.8%)	71 (88.8%)
OPL	33 (41.3%)	48 (60.0%)	55 (68.8%)	19 (23.8%)	25 (31.3%)	35 (43.8%)
ONL	33 (41.3%)	41 (51.3%)	47 (58.8%)	46 (57.5%)	53 (66.3%)	64 (80.0%)
Total	185 (38.5%)	255 (53.1%)	303 (63.1%)	239 (49.8%)	288 (60.0%)	336 (70.0%)

The spread of statistically significant differences across the layers of the retina demonstrates the massive impact in the entire retina of the three genes present in the mouse model of the AD group. Since the retina is the visible part of the CNS, these results put forward the hypothesis that there is a broad impact in the brain, and that it can be assessed through the retina.

While the found differences are notoriously spread across different layers of the retina (Table 1), the INL stands out as the layer presenting the highest differences at both time-points and across the three levels of significance.

Table 2 discloses all texture features presenting statistically significant differences between groups at both time-points, i.e. at the age of one and two-months-old, and at the same locations (same quadrants). While it is quite notorious the widespread differences across the several layers and the imaged area, as shown by the number of quadrants involved per textures feature and layer, the INL stands out again because of the highest level of significance and the extension of the differences spreading through the entire imaged area of the retina.

Also of notice, is the steady increase in the number of statistically significant differences from the first to the second time-points in all layers but the OPL.

Furthermore, even though the total number of features presenting statistically significant differences increased from 306 to 330, $\sim$8% increase, the notorious fact is

Table 2: Features with statistically significant differences between wild-type and transgenic mice groups at both time-points. The green-coloured circles (●) represent a p-value ≤ 0.05, the orange-coloured squares (■) show p-values ≤ 0.01 and the red-coloured asterisks (✱) represent a p-value ≤ 0.001. The number of symbols in each time-point identifies the number of quadrants where the significance was observed for each of the features shown.

Layer	Feature	Age (months) 1	Age (months) 2
RNFL	Entropy	■●	✱✱
	Dissimilarity	✱✱●	✱✱✱
	Inertia	✱✱■	✱✱✱
	Cluster Prominence	✱	■
	Sum Entropy	✱	●
	Difference Variance	✱✱■	✱✱✱
	Difference Entropy	✱✱■	✱✱✱
	IMC1	■■	✱●
GCL	Homogeneity	●■	●●
	Uniformity	■✱	■■
	Entropy	✱✱	✱✱
	Dissimilarity	✱✱✱	✱✱✱
	Inertia	●✱✱✱	✱✱✱✱
	Autocorrelation	■✱	✱✱
	Cluster Shade	■✱	✱✱
	Maximum Probability	■✱	■■
	Sum Of Squares	✱✱	✱✱
	Sum Average	✱✱	✱✱
	Sum Variance	✱✱	✱✱
	Difference Variance	●✱✱✱	✱✱✱✱
	Difference Entropy	●✱✱✱	✱✱✱✱
	IMC1	■✱✱✱	✱✱✱✱
	INN	■	●
	IDN	■	●
IPL	Homogeneity	■✱	■✱
	Uniformity	■✱	●●
	Entropy	●	●
	Dissimilarity	●●✱✱	✱■✱✱
	Inertia	●■✱✱	✱✱✱✱
	Correlation	■✱	■✱
	Autocorrelation	✱✱	✱✱
	Cluster Prominence	●■	●✱
	Maximum Probability	●	■
	Sum Of Squares	✱✱	✱✱
	Sum Average	✱✱	✱✱
	Sum Variance	✱✱	✱✱
	Sum Entropy	●✱	●✱
	Difference Variance	●■✱✱	✱✱✱✱
	Difference Entropy	●■✱✱	✱■✱✱
	IMC1	■✱✱	✱✱✱
	IMC2	■✱	■✱
	INN	■✱	■✱
	IDN	■✱	■✱

Layer	Feature	Age (months) 1	Age (months) 2
INL	Homogeneity	■✱✱✱	■✱✱✱
	Uniformity	✱✱	■■
	Dissimilarity	■✱✱✱	✱✱✱✱
	Inertia	■✱✱✱	✱✱✱✱
	Correlation	■✱✱✱	■✱✱✱
	Autocorrelation	■■✱✱	✱✱✱✱
	Cluster Prominence	✱✱✱✱	■✱✱✱
	Maximum Probability	■■	●●
	Sum Of Squares	●●✱✱	✱✱✱✱
	Sum Average	●●✱✱	✱✱✱✱
	Sum Variance	●●✱✱	✱✱✱✱
	Sum Entropy	■✱✱✱	✱✱✱✱
	Difference Variance	■✱✱✱	✱✱✱✱
	Difference Entropy	■✱✱✱	✱✱✱✱
	IMC1	✱✱✱✱	✱✱✱✱
	IMC2	■✱✱✱	✱✱✱✱
	INN	●✱✱✱	■✱✱✱
	IDN	●✱✱✱	■✱✱✱
OPL	Homogeneity	■	✱
	Entropy	✱	●
	Dissimilarity	■	■
	Inertia	■	■
	Correlation	✱	✱
	Autocorrelation	■●	●✱
	Cluster Prominence	■✱	✱●
	Sum Of Squares	■	●
	Sum Average	■	●
	Sum Variance	■	●
	Sum Entropy	✱✱✱	●✱■
	Difference Variance	■	■
	Difference Entropy	■	■
	IMC1	✱✱✱✱	✱✱✱✱
	IMC2	✱✱✱	✱●●
	INN	■	✱
	IDN	■	✱
ONL	Homogeneity	✱✱	✱✱
	Uniformity	■✱	■✱
	Dissimilarity	✱■✱✱	■✱✱✱
	Inertia	✱■✱✱	✱✱✱✱
	Correlation	✱✱	✱✱
	Autocorrelation	●	✱
	Cluster Prominence	✱✱	✱✱
	Maximum Probability	✱	●
	Sum Entropy	✱✱	✱✱
	Difference Variance	✱■✱✱	✱✱✱✱
	Difference Entropy	✱■✱✱	■✱✱✱
	IMC1	■■✱✱	●✱✱✱
	IMC2	✱✱	✱✱
	INN	✱✱	✱✱
	IDN	✱✱	✱✱

that there was a significant increase at the highest significance level (p-value ≤ 0.001) with 185 at the age of one-month-old and 239 at the age of two-months-old, an increase of almost 30%.

Table 3 further details these findings by presenting the number of features at each time-point, the number of those that showed significant differences at both time-points ($T01 \cap T02$) (detailed in table 2) and those that showed at only one of the time-points, $T01 - (T01 \cap T02)$ and $T02 - (T01 \cap T02)$, respectively those present only at the age of one-month-old and those present at the age of two-months-old.

As in tables 1 and 2, table 3 shows that the INL is the layer where texture features consistently present statistically significant differences at both time-points, while the RNFL is the one presenting the least consistent differences.

From the progression point of view, two layers stand out in table 3, the IPL and the ONL. Data in table 3 demonstrates that in these layers only 2 out of 47 and 9 out of 47 features, respectively for the IPL and ONL, ceased to show statistically significant differences at the age of two-months-old while having shown at the age of one-month-old. On the other hand, 21 and 26 features show differences at the age of two-months-old without having done so at the age of one-month-old, being strong candidates for biomarkers of progression and showing these may be the layers undergoing the most notorious changes. These features are disclosed in table 4, where it is notorious that the majority of these features present statistically significant differences at the highest significance level.

Table 3: Total number of significant features for each data set, from left to right the number of: significant features at the age of one-month-old; significant features at the age of two-months-old; significant features in both time-points; significant features that became not statistically significant at the age of two-months-old; significant features at the age of two-months-old that were not statistically significant at the age of one-month-old.

	T01	T02	$T01 \cap T02$	$T01 - (T01 \cap T02)$	$T02 - (T01 \cap T02)$
RNFL	35	39	18	17	21
GCL	50	61	39	11	22
IPL	47	66	45	02	21
INL	69	71	68	01	03
OPL	55	35	26	29	09
ONL	47	64	38	09	26
Total	303	336	234	69	102

Table 4: Features with statistically significant differences between wild-type and transgenic mice groups at two-months-old that were not present in the previous month, for the IPL and ONL layers. Following the same display scheme described in table 2.

Layer	Feature	Quadrants
IPL	Homogeneity	■
	Entropy	●
	Correlation	✱
	Autocorrelation	✱✱
	Cluster Shade	■✱■✱
	Cluster Prominence	■
	Sum of Squares	✱✱
	Sum Average	✱✱
	Sum Variance	✱✱
	Sum Entropy	✱
	IMC1	●
	IMC2	✱
	INN	■
	IDN	✱

Layer	Feature	Quadrants
ONL	Homogeneity	✱
	Uniformity	●
	Entropy	■
	Correlation	✱
	Autocorrelation	●■✱
	Cluster Prominence	■
	Maximum Probability	■
	Sum of Squares	●●✱✱
	Sum Average	●●✱✱
	Sum Variance	●●✱✱
	Sum Entropy	●✱
	IMC2	✱
	INN	✱
	IDN	✱

4 Discussion

The need for the early detection of changes unfolding in the CNS due to Alzheimer's disease is of utmost, and increasing, importance as life expectancy is steadily increasing [1] and the prevalence in people aged 65 and older reached the two figures in

2019 in the USA [2]. Furthermore, it is hypothesised that AD has advanced over two decades when detected by state-of-the-art means [4,5], hampering the access to the first pathophysiological changes caused by AD and tracking their progress. While the use of the retina as a window into the CNS has been used, mostly resorting to thickness measurements, these studies should be taken into account carefully as the generally claimed thinning of the retina is not exclusive to AD.

In this study, we address changes in the retina of the triple-transgenic mouse model of AD, at the ages of one and two-months-old, by comparing those with a WT group at the same age. We performed a texture analysis of the MVF image for each of the inner six retinal layers (from the RNFL to the ONL) to identify differences in the retina between two mice groups. These images were then split into 24×24 blocks, that were individually analysed by computing local texture metrics (GLCM). We followed a prior work on humans that demonstrated the ability of texture analysis in distinguishing between AD patients, Parkinson's patients, and healthy controls [15], and previous results in a smaller study involving this mouse model of AD [20].

A massive distinction between WT and 3×Tg-AD was found across the different layers of the retina and spreading over the imaged area. The most relevant differences between groups were found at the INL with a significant number of statistically significant differences at both time-points, showing that texture features are consistent in showing the differences between groups. Also, the progression of AD is clear from changes within the IPL and ONL layers between the to time-points.

It is of particular importance to notice that this study demonstrates the potential use of texture for the detection and progression assessment of AD, as suggested by found differences at each time-point and the significant differences found at the IPL and ONL from the age of one to the age to two-months-old.

The limitation of the present study arises from the substantial differences found at the first time-point, at the age of one-month-old, where the two groups already present clear differences spread over the retina, which precludes the identification of changes associated with the onset of the AD. Another limitation is due to the estimation of layer interfaces based on the relative thickness known from the histology of mice. Nevertheless, these interfaces were visually assessed through a substantial sampling over the B-scans, and none showed to be incorrect requiring any correction. Furthermore, tests were conducted by artificially changing the location of the interfaces to assess the consistency of the findings to these changes that kept demonstrating the same differences between groups.

The differences between groups found in this study suggest that the 3×Tg-AD model may be inappropriate to study early changes associated with the AD and other animal models should be tested following the same path and rationale. Moreover, these results also suggest that the human genes present in these transgenic mice may have an impact on the neurodevelopment of offspring which would justify the significant changes found at the age of one-month-old.

Further work on this subject will focus on a new mouse model of AD and on its study of early changes in the retina and the brain. Nonetheless, the found differences shed light on changes unfolding in the retina associated with the AD, its progression, and allow to state with confidence that texture biomarkers from OCT data convey information on CNS changes.

5 Conclusions

The present study sheds light on the possibility of using texture features as biomarkers of CNS changes associated with the AD using a non-invasive, *in vivo* and *in situ* optical imaging system, the OCT. In this study, we provide evidence suggesting the neuroretina, the visible part of the CNS, presents distinct characteristics for WT (controls) and 3×Tg-AD mice, that these differences are present early in life (at the age of one-month-old), and that differences progress from the age of one to the age of two-months-old.

References

1. Alzheimer Association, Alzheimer's and Dementia pp. 1–88 (2019)
2. United Nations, World Population Prospects 2019. 141 (2019)
3. H. Shah, E. Albanese, C. Duggan, I. Rudan, K.M. Langa, M.C. Carrillo, K.Y. Chan, Y. Joanette, M. Prince, M. Rossor, S. Saxena, H.M. Snyder, R. Sperling, M. Varghese, H. Wang, M. Wortmann, T. Dua, The Lancet Neurology **15**(12), 1285 (2016). DOI 10.1016/S1474-4422(16)30235-6
4. C.R. Jack, V.J. Lowe, S.D. Weigand, H.J. Wiste, M.L. Senjem, D.S. Knopman, M.M. Shiung, J.L. Gunter, B.F. Boeve, B.J. Kemp, M. Weiner, R.C. Petersen, Brain **132**(5), 1355 (2009). DOI 10.1093/brain/awp062
5. D.J. Harper, M. Augustin, A. Lichtenegger, J. Gesperger, T. Himmel, M. Muck, C.W. Merkle, P. Eugui, S. Kummer, A. Woehrer, M. Glösmann, B. Baumann, pp. 1–27 (2019)
6. G.B. Frisoni, M. Boccardi, F. Barkhof, K. Blennow, S. Cappa, K. Chiotis, J.F. Démonet, V. Garibotto, P. Giannakopoulos, A. Gietl, O. Hansson, K. Herholz, C.R. Jack, F. Nobili, A. Nordberg, H.M. Snyder, M. Ten Kate, A. Varrone, E. Albanese, S. Becker, P. Bossuyt, M.C. Carrillo, C. Cerami, B. Dubois, V. Gallo, E. Giacobini, G. Gold, S. Hurst, A. Lönneborg, K.O. Lovblad, N. Mattsson, J.L. Molinuevo, A.U. Monsch, U. Mosimann, A. Padovani, A. Picco, C. Porteri, O. Ratib, L. Saint-Aubert, C. Scerri, P. Scheltens, J.M. Schott, I. Sonni, S. Teipel, P. Vineis, P.J. Visser, Y. Yasui, B. Winblad. Strategic roadmap for an early diagnosis of Alzheimer's disease based on biomarkers (2017). DOI 10.1016/S1474-4422(17)30159-X
7. A. London, I. Benhar, M. Schwartz, Nature Reviews Neurology **9**(1), 44 (2013). DOI 10.1038/nrneurol.2012.227
8. S.N. Svetozarskiy, S.V. Kopishinskaya, Sovremennye Tehnologii v Medicine **7**(1), 116 (2015). DOI 10.17691/stm2015.7.1.14
9. S.S. Ong, P. Murali Doraiswamy, E.M. Lad. Controversies and future directions of ocular biomarkers in Alzheimer disease (2018). DOI 10.1001/jamaneurol.2018.0602
10. J.C. De La Torre. Is Alzheimer's disease a neurodegenerative or a vascular disorder? Data, dogma, and dialectics (2004). DOI 10.1016/S1474-4422(04)00683-0
11. V.T. Chan, Z. Sun, S. Tang, L.J. Chen, A. Wong, C.C. Tham, T.Y. Wong, C. Chen, M.K. Ikram, H.E. Whitson, E.M. Lad, V.C. Mok, C.Y. Cheung, Ophthalmology **126**(4), 497 (2019). DOI 10.1016/j.ophtha.2018.08.009
12. J. den Haan, F.D. Verbraak, P.J. Visser, F.H. Bouwman, Alzheimer's and Dementia: Diagnosis, Assessment and Disease Monitoring **6**, 162 (2017). DOI 10.1016/j.dadm.2016.12.014
13. C.Y. lui Cheung, M.K. Ikram, C. Chen, T.Y. Wong, Progress in Retinal and Eye Research **57**, 89 (2017). DOI 10.1016/j.preteyeres.2017.01.001
14. P. Guimarães, P. Rodrigues, C. Lobo, S. Leal, J. Figueira, P. Serranho, R. Bernardes, Computerized Medical Imaging and Graphics **38**, 381 (2014). DOI 10.1016/j.compmedimag.2014.02.003
15. A. Nunes, G. Silva, C. Duque, C. Januário, I. Santana, A.F. Ambrósio, M. Castelo-Branco, R. Bernardes, PLoS ONE **14**(6), 1 (2019). DOI 10.1371/journal.pone.0218826
16. H. Ferreira, J. Martins, A. Nunes, P.I. Moreira, M. Castelo-Branco, A.F. Ambrósio, P. Serranho, R. Bernardes, in XV Mediterranean Conference on Medical and Biological Engineering and Computing – MEDICON 2019. MEDICON 2019. IFMBE Proceedings, ed. by J. Henriques, N. N. (Springer, Cham, 2020), pp. 1816–1821. DOI 10.1007/978-3-030-31635-8
17. S. Oddo, A. Caccamo, M. Kitazawa, B.P. Tseng, F.M. LaFerla, Neurobiology of Aging **24**(8), 1063 (2003). DOI 10.1016/j.neurobiolaging.2003.08.012

18. S. Oddo, A. Caccamo, J.D. Shepherd, M.P. Murphy, T.E. Golde, R. Kayed, R. Metherate, M.P. Mattson, Y. Akbari, F.M. LaFerla, Neuron **39**(3), 409 (2003). DOI 10.1016/S0896-6273(03)00434-3
19. A. Nunes, A.F. Ambrósio, M. Castelo-Branco, R. Bernardes, Proceedings - 2018 IEEE 18th International Conference on Bioinformatics and Bioengineering, BIBE 2018 pp. 41–46 (2018). DOI 10.1109/BIBE.2018.00016
20. R. Bernardes, G. Silva, S. Chiquita, P. Serranho, A.F. Ambrósio, in 14th International Conference on Image Analysis and Recognition (ICIAR) (2017). DOI 10.1007/978-3-319-59876-5
21. C. Dysli, V. Enzmann, R. Sznitman, M.S. Zinkernagel, Translational Vision Science and Technology **4**(4), 9 (2015). DOI 10.1167/tvst.4.4.9
22. K.H. Kim, M. Puoris'haag, G. Maguluri, Y. Umino, K. Cusato, R. B Barlow, J. de Boer, Journal of vision **8**, 17.1 (2008). DOI 10.1167/8.1.17
23. A.G. Roy, S. Conjeti, S.P.K. Karri, D. Sheet, A. Katouzian, C. Wachinger, N. Navab, Biomedical Optics Express **8**(8), 3627 (2017). DOI 10.1364/boe.8.003627
24. A. Baghaie, Z. Yu, R.M. D'Souza, Quantitative imaging in medicine and surgery **5**(4), 603 (2015). DOI 10.3978/j.issn.2223-4292.2015.07.02
25. A. Meyer-Base, Patter Recognition in Medical Imaging (Elsevier Inc, 2004). DOI 10.1016/B978-0-12-493290-6.X5000-7
26. R.M. Haralick, K. Shanmugam, I. Dinstein, IEEE Transaction on Systems, Man and Cybernetics **SMC-3**(6), 610 (1973). DOI 10.1109/TSMC.1973.4309314
27. L.K. Soh, C. Tsatsoulis, IEEE Transactions on Geoscience and Remote Sensing **37**(2 I), 780 (1999). DOI 10.1109/36.752194
28. R.M. Haralick, Proceedings of the IEEE **67**(5), 786 (1979). DOI 10.1109/PROC.1979.11328
29. R.W. Conners, M.M. Trivedi, C.A. Harlow, Computer Vision, Graphics, & Image Processing **25**(3), 273 (1984). DOI 10.1016/0734-189x(84)90197-x
30. D.A. Clausi, Canadian Journal of Remote Sensing **28**(1), 45 (2002). DOI 10.5589/m02-004